Cell Reports
Physical Science

CellPress

Article

Enhancing Singlet Oxygen Generation by Self-Assembly of a Porphyrin Entrapped in Supramolecular Fibers

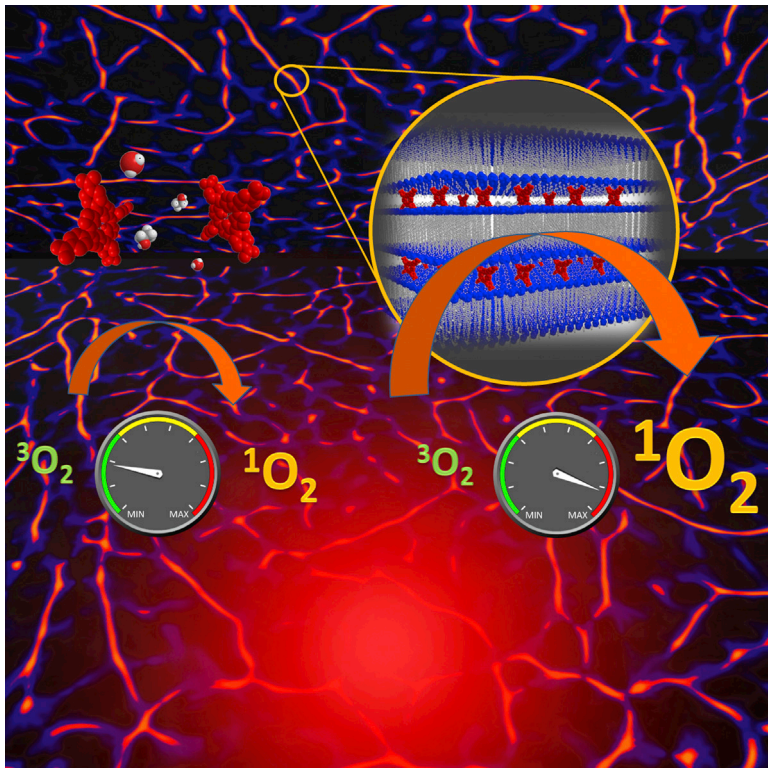

Oxygen can be made into a reactive form—singlet oxygen—upon excitation. It is useful for chemical reactions, treating water impurities, and aiding in medicinal therapy. Here, Samperi et al. report the preparation of nanofibers that generate this form of oxygen far more efficiently than the dissolved photosensitizer used until now.

Mario Samperi, David Limón, David B. Amabilino, Lluïsa Pérez-García

david.amabilino@nottingham.ac.uk (D.B.A.)
lluisa.perezgarcia1@nottingham.ac.uk (L.P.-G.)

HIGHLIGHTS

Facile preparation of hybrid functional supramolecular nanomaterials

High-efficiency singlet oxygen formation by hybrid nanofibers upon irradiation

Rate of singlet oxygen is 14-fold higher from fibers than in solution

Super-resolution radial fluctuations microscopy shows chromophore location precisely

Samperi et al., Cell Reports Physical Science 1, 100030
March 25, 2020
https://doi.org/10.1016/j.xcrp.2020.100030

Please cite this article in press as: Samperi et al., Enhancing Singlet Oxygen Generation by Self-Assembly of a Porphyrin Entrapped in Supramolecular Fibers, Cell Reports Physical Science (2020), https://doi.org/10.1016/j.xcrp.2020.100030

Cell Reports
Physical Science

CellPress

Article

Enhancing Singlet Oxygen Generation by Self-Assembly of a Porphyrin Entrapped in Supramolecular Fibers

Mario Samperi,[1,2] David Limón,[3,4] David B. Amabilino,[2,*] and Lluïsa Pérez-García[1,5,*]

SUMMARY

Singlet oxygen (SO) is one of the reactive oxygen species that is effective in various uses, including performing chemical reactions, treating water impurities, and aiding in medicinal therapy. The generation of SO is often efficient in solution, although generation from the solid phase in nanomaterials is less reliable. Here, we report the preparation of hybrid supramolecular materials that incorporate a photosensitizer within their nanostructured fibers and demonstrate their high efficiency in promoting SO formation. The incorporation of tetrakis(4-carboxyphenyl)porphyrin within the nanofibers of a bis-imidazolium gelator was proved by various techniques, including super-resolution radial fluctuations (SRRF) microscopy, which shows the location of the chromophore precisely. SO is generated from the dispersed nanofibers far more efficiently than the dissolved porphyrin; a 14-fold higher rate is observed initially. These results point to an effective approach to the generation of SO for several applications, from optimizing synthetic protocols to photomedicine.

INTRODUCTION

The generation and understanding of the formation of reactive oxygen species (ROS), and in particular singlet oxygen (SO), are important in a number of areas of science and technology.[1–4] They play a vital part in biochemical processes, such as cell signaling,[5] as well as in biomedical science.[6] In synthetic systems, they are useful for preparative methods in organic chemistry.[7–9] The formation of SO is generally achieved by the action of light on a photosensitizer that activates the oxygen, often with a high quantum yield in non-aqueous solvents.[10,11] However, in water, the overall efficiency of the SO generation process is low.

A simple picture of photosensitizer excitation followed by energy transfer from the excited state to triplet oxygen forming SO implies that the tuning of the excited states through covalent modification of the chromophore would allow optimization of the efficiency of the energy transfer process. However, the environment of the chromophore in materials also plays a role, whose understanding and prediction is an enormous challenge because some immobilized photosensitizers show a slightly improved generation of SO compared with their dissolved equivalents, while others have poorer conversion. The supramolecular structure has a great effect on the process.[12–14] Therefore, one way to influence the efficiency of SO generation is through tailoring the environment of a given chromophore. For example, incorporation of a boron dipyrromethene (BODIPY) photosensitizer into micelles resulted in an increase in photodynamic therapy (PDT) efficacy,[15] as occurs in a

[1]School of Pharmacy, University of Nottingham, University Park, Nottingham NG7 2RD, UK

[2]School of Chemistry, The GSK Carbon Neutral Laboratories for Sustainable Chemistry, University of Nottingham, Triumph Road, Nottingham NG7 2TU, UK

[3]Institut de Nanociència i Nanotecnologia (IN2UB), Barcelona, Spain

[4]Departament de Farmacologia, Toxicologia i Química Terapèutica, Universitat de Barcelona, Barcelona, Spain

[5]Lead Contact

*Correspondence: david.amabilino@nottingham.ac.uk (D.B.A.), lluisa.perezgarcia1@nottingham.ac.uk (L.P.-G.)

https://doi.org/10.1016/j.xcrp.2020.100030

Cell Reports
Physical Science

photooxidase mimic formed by the assembly of a phthalocyanine and an amphiphilic amino acid,[16] and in phthalocyanine functionalized gold nanoparticles.[17]

Here, we use porphyrins for producing SO, as they are efficient photosensitizers, a feature that has made them useful for generating SO (the main type of ROS formed) for synthetic chemistry[18–20] and PDT.[21–24] To these ends, apart from using them in homogeneous solution, different porphyrin-containing vehicles have been developed, such as polyacrylamide nanoparticles,[25] silica nanoparticles,[26] and silicon microparticles.[27] The use of these vehicles has proven that not only is the porphyrin type important but also its surroundings. The enhanced generation of SO from immobilized photosensitizers has been observed in polymerized zinc porphyrazine nanospheres,[28] while immobilized porphyrins and phthalocyanines generate SO for the degradation of pollutants.[29] A specific case is the reaction of metoprolol with SO by a reaction involving the photoexcitation of a porphyrin immobilized on silica gel that shows different kinetics of SO generation (exponential rather than pseudo-first order for a solution analog) to the dissolved photosensitizer.[30] Porphyrins immobilized on nanoparticles can have impaired SO generation (compared with freely dissolved compounds) that depends on the linker and the platform.[31]

We reasoned that incorporating porphyrins into a lamellar-type amphiphile array could enhance SO generation, and herein demonstrate the ability of a supramolecular hydrogel to incorporate into its fibrillar network a porphyrin derivative, which shows greatly enhanced generation of SO compared with the molecularly dissolved porphyrin in solution. This supramolecular system is unlike other gel photosensitizer-incorporated systems, in which the porphyrins are potentially held non-specifically.[32–35] Also, in our hybrid system, we show how this assembly allows the imaging of the gel in its hydrated state and permits investigation *in situ* of its real 3-dimensional (3D) network with super-resolution radial fluctuations (SRRF) microscopy.[36]

RESULTS

Self-Assembly of the Hybrid Material Gel@TCPP

The molecular gelator we use here is the gemini imidazolium-based amphiphile 1·2Br (Figure 1) that self-assembles in water-ethanol mixtures, leading to the formation of supramolecular (physical) gels.[37] This amphiphile is widely soluble in ethanol and the addition of water, which acts as an anti-solvent for the system, triggers the self-assembly and fiber formation.[38] We have also demonstrated that the aggregation process of this amphiphile, which takes place under conditions in which the system is far from equilibrium, is remarkably affected by water-ethanol proportion and temperature, which tune the kinetics of nucleation and growth of the fibers and define the morphology and the physicochemical properties of the final gels.[39] This amphiphile packs within the fibers in lamellae, formed of bilayers of amphiphilic molecules with interdigitated alkyl chains that, stacking on top of each other, lead ultimately to multilayer nanostructured fibers.

In the present study, we demonstrate the ability of 1·2Br to incorporate the sodium salt of the 5,10,15,20-tetrakis(4-carboxylatephenyl)porphyrin (TCPP) during the process of gel formation, trapping the guest molecules within the multilayer structure of the fibers. The phase diagram of 1·2Br shows that gels can be obtained as a function of both amphiphile concentration (1–12 mM) and water:ethanol ratio (1:1–9:1).[39] We used an amphiphile concentration of 12 mM to allow the maximum photosensitizer

Cell Reports
Physical Science

CellPress

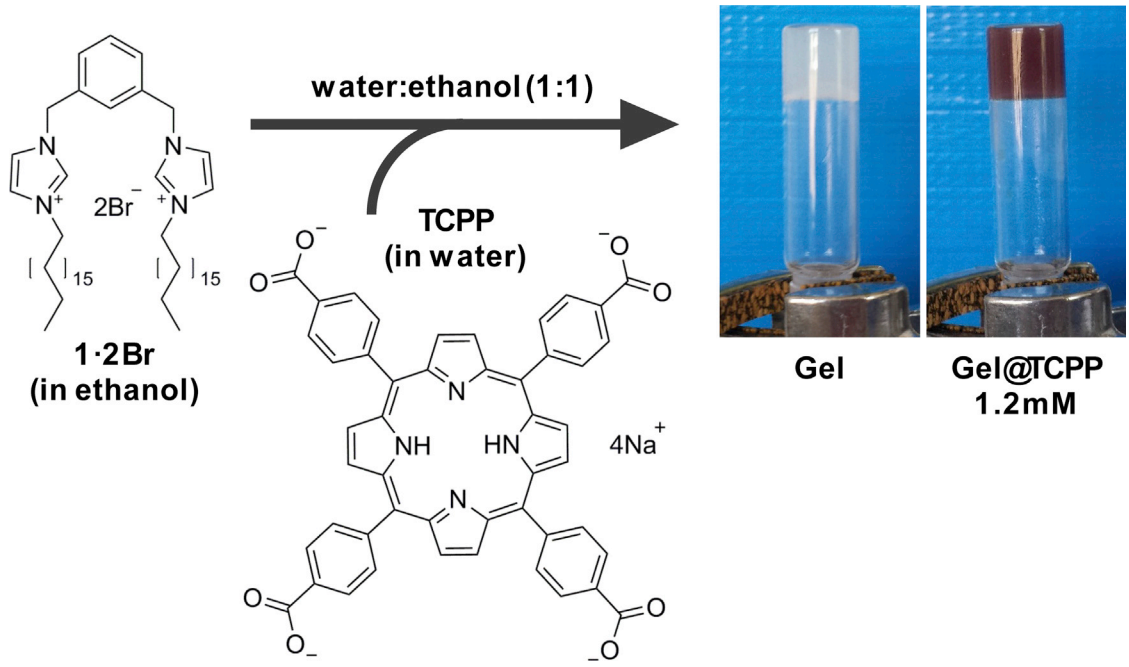

Figure 1. Preparation of the Hybrid Gel@TCPP

Chemical structures of the gelator **1**·2Br and the porphyrin TCPP as sodium salt, and schematic representation of sample preparation with and without porphyrin, leading to the final gels.

loading capacity and found that a solvent ratio of 1:1 was most suited for the formation of hybrid gels (Figure 1; Video S1).

The gel without porphyrin forms readily by the addition of water to an ethanolic solution of 1·2Br to give a final amphiphile concentration of 12 mM and water:ethanol ratio 1:1. The resulting gel forms after ~3 min (Figure S1, gray bar), is quite opaque and robust, and is stable over several months. To obtain the gels with incorporated porphyrin (Gel@TCPP), an aqueous solution of TCPP as sodium salt was added to the ethanolic solution of 1·2Br. Gels were loaded with increasing amounts of porphyrin up to a final concentration of 1.2 mM, forming homogeneous gels which become more brown as the porphyrin content increases (Figure 1). Above this TCPP concentration, unstable and inhomogeneous gels were formed that show the typical gel texture together with solid material that obviously contains the porphyrin. For concentrations of TCPP up to 1.2 mM, the presence of the porphyrin does not prevent the self-assembly of 1·2Br, but rather affects the gelation time, the morphology of the fibers, and the mechanical and physicochemical properties of the final gels (*vide infra*). The Gel@TCPPs showed gradually quicker gelation time as the porphyrin concentration increases up to 1.2 mM, producing gel in ~2.5 min for the sample with the highest amount of TCPP (Figure S1, red bars).

The mechanical properties of the gels were assessed by a rheological analysis performed as a function of porphyrin loading. The viscoelastic parameters obtained from stress sweep experiments (Figure S2) are shown in Table S1. For all of the samples analyzed, a common behavior was the prevalence of the storage modulus (G′) over the loss modulus (G″), which highlights the typical elastic response for these gels.[37] In particular, shear stress profiles obtained from gels with and without TCPP show high moduli values at zero-shear stress and wide linear viscoelastic regimes; however, storage and loss moduli increase as the TCPP content

Cell Reports
Physical Science

increases, indicating that the gradual increase in resistance to deformation may be related to the incorporation of the porphyrin within the fibrillar network. Moreover, the critical stress values (crossover points when G′ = G″; Table S1) indicate that the gel obtained with the higher loading of TCPP (1.2 mM) is significantly more resistant to rupture than those having a lower porphyrin content (gel with no TCPP, 0.012 and 0.12 mM). These features clearly suggest that TCPP is actively participating in the self-assembly process, contributing to build up the fibrillar network of the gels, and enhancing their strength, particularly at high TCPP concentrations.

TIRF and SRRF for Imaging *In Situ* of the Real Hydrated Fibrillar Network

The incorporation of the porphyrin into the fibers was confirmed by total internal reflection fluorescence (TIRF) microscopy, a technique that allows characterization of the bulk gels directly in their hydrated state *in situ* by acquiring the porphyrin fluorescence emission arising from the excitation of a thin layer of the sample, typically between 100 and 200 nm.[40] Samples were prepared directly on a glass slide equipped with a 10-well compartmentalization block, which allowed us to form the gel *in situ* and perform the imaging directly without any further sample manipulation. The images in Figure 2, recorded using the "16-frames averaging" option (Zeiss) and a high-resolution camera (complementary metal-oxide semiconductor [CMOS]) for data acquisition, show the gels with a concentration of 12 mM in 1·2Br and different TCPP loading. They reveal the real hydrated fibrillar network and highlight the influence of the porphyrin on the morphology of the fibers and their mutual interconnections within the gel. All 3 samples analyzed with this fluorescence imaging technique show that the porphyrin is practically completely trapped by the fibers, with negligible fluorescence in the interstitial areas. In this regard, release experiments performed on Gel@TCPP 1.2 mM (see Figure S3) show that no porphyrin is released from the fibrillar network after 6 days, suggesting that the entire amount of TCPP used for gel preparation is totally incorporated into the fibers. TIRF images show highly interconnected fibrillar networks, having different features as a function of the porphyrin load (Figure 2).

The gel with the lowest TCPP concentration used (Gel@TCPP 0.012 mM; Figure 2A) shows a very dense network of thin and straight micrometric-long fibers that run across the gel with no particular 3D-ordered arrangement; a tightly packed mesh forms with small interstitial areas. When the porphyrin load is increased to 0.12 mM (Figure 2C), wider fibers are formed that bend and intertwine within an apparently less dense fibrillar network with bigger interstitial areas than the gel with a lower concentration of porphyrin where straighter fibers with smaller voids are observed. These features are sharper when a higher porphyrin concentration is used (Gel@TCPP 1.2 mM; Figure 2E), with the sample displaying fibers that are less well defined than the other composites, gathering together to form large bundles and large clusters of fibers. These images, acquired in standard TIRF mode, show the conventional spatial resolution limit of fluorescence microscopy, in which the evaluation of the cross-section of the fibers gives minimum values of apparent full width at half-maximum (FWHM) of ≈280 nm, in line with the Abbe diffraction limit given by the porphyrin emission at 650 nm. Nevertheless, the analysis of the apparent width of the fibers for the 3 samples (Figures 2B, 2D, and 2F) shows an average value of 373 nm for the gel fibers obtained with the lowest amount of TCPP, which becomes larger as the porphyrin content increases (479 and 495 nm for Gel@TCPP 0.12 mM and Gel@TCPP 1.2 mM, respectively). The polydispersity is also affected by porphyrin loading; the FWHM values for the curves in Figure 2 are 107, 100, and 136 nm from lowest to highest TCPP content (with the latter value

Cell Reports
Physical Science

CellPress

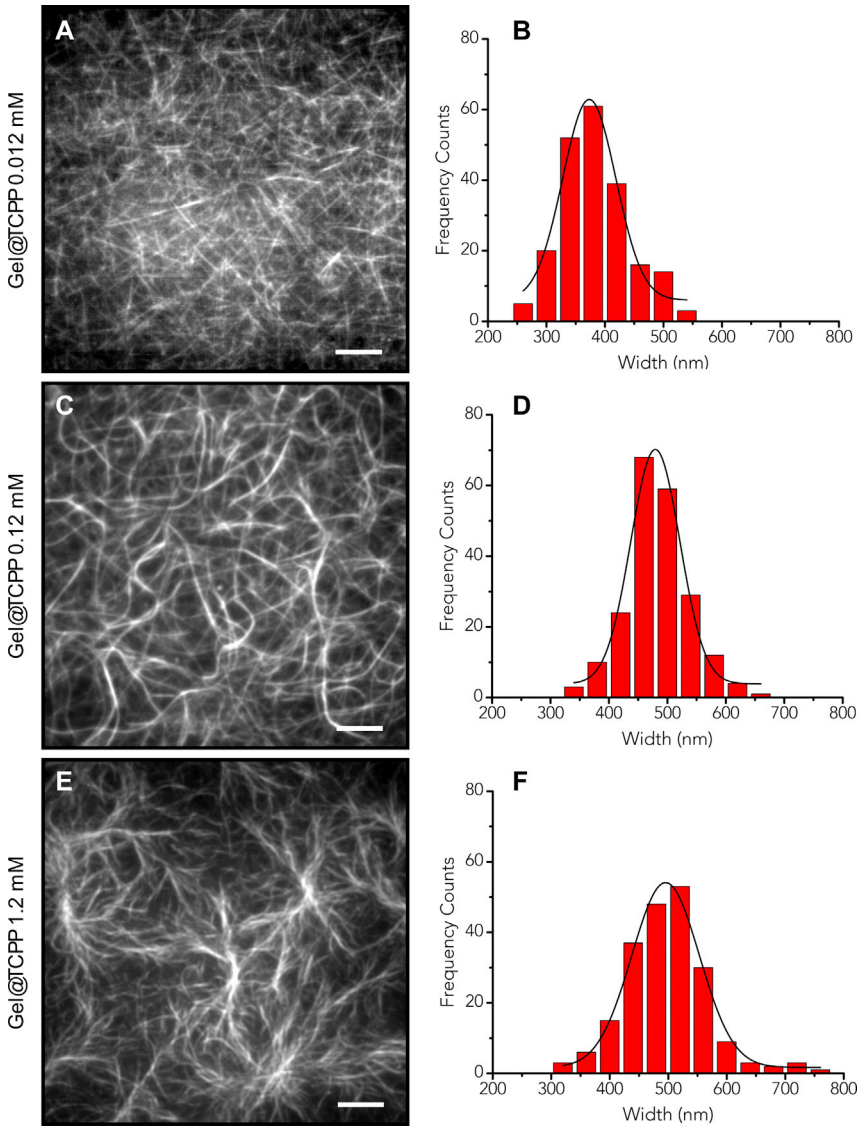

Figure 2. Morphology of the 3D Network of Gel@TCPP *In Situ*

(A–F) Fluorescence images acquired in TIRF mode with intensity averaging of 16 frames of gel samples in their hydrated as-formed state having concentrations of 1·2Br 12 mM and TCPP 0.012 mM (A), 0.12 mM (C), and 1.2 mM (E) in a water-ethanol ratio 1:1. Corresponding distribution histograms of fiber apparent width (B, D, and F) obtained from FWHM measurement of the fluorescence intensity cross-section. The scale bars represent 5 μm.

being a partial consequence of bundling, as shown in higher-resolution imaging; see below).

Seeking further insight as to the effect of the porphyrin on fiber morphology, we analyzed the gel structures using SRRF microscopy,[36] a recently developed analytical approach that provides super-resolution information from the temporal variation of the fluorescence intensity in datasets acquired in the illumination condition that is orders of magnitude lower than standard single-molecule localization methods (photo-activated localization microscopy [PALM] and stochastic optical reconstruction microscopy [STORM]).[41] To perform SRRF analysis, a sequence of 100 frames

Please cite this article in press as: Samperi et al., Enhancing Singlet Oxygen Generation by Self-Assembly of a Porphyrin Entrapped in Supramolecular Fibers, Cell Reports Physical Science (2020), https://doi.org/10.1016/j.xcrp.2020.100030

Cell Reports
Physical Science

CellPress

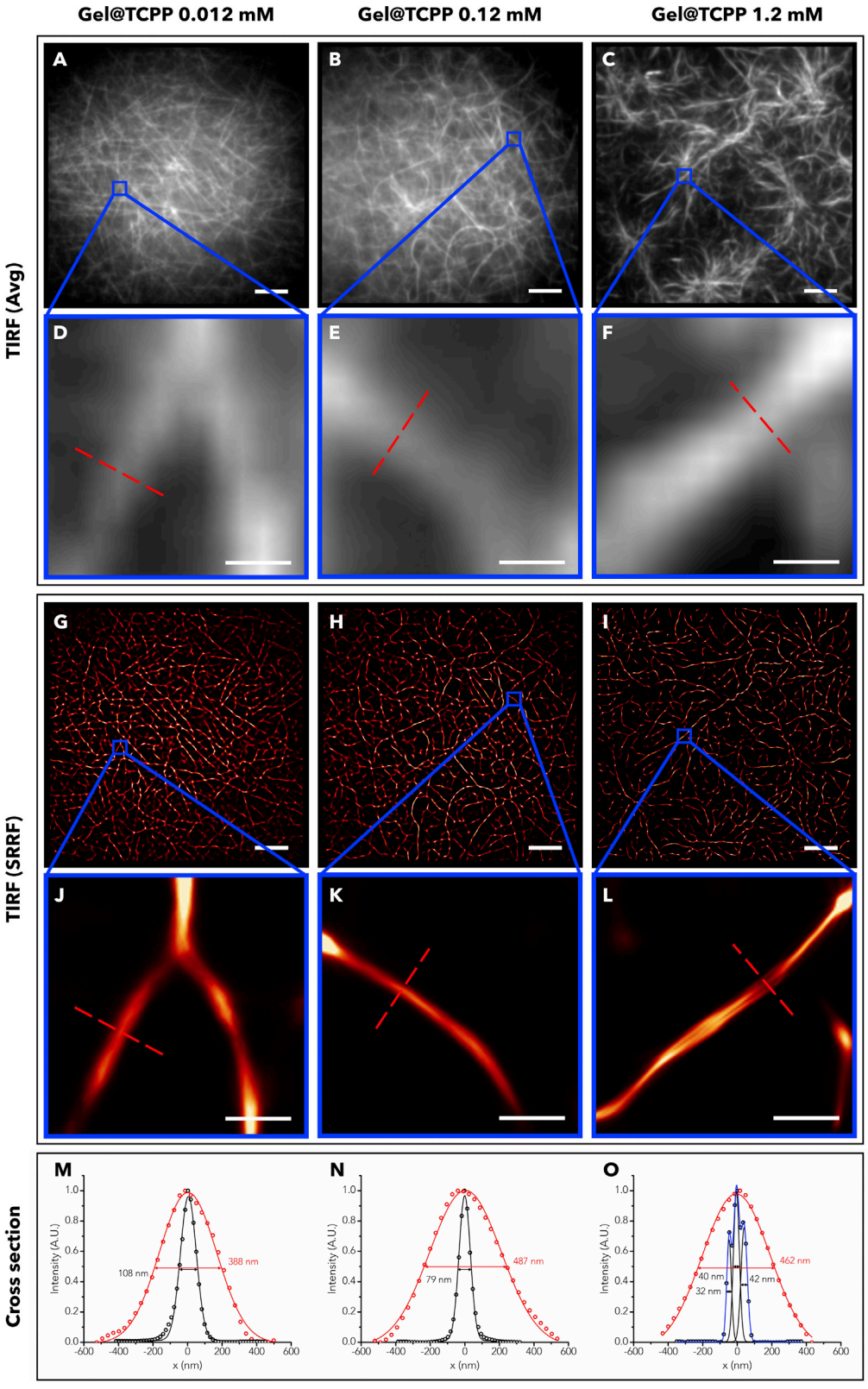

Cell Reports
Physical Science

was acquired for a given sample in standard TIRF mode and recorded with a high-sensitivity camera (using an electron-multiplying charge-coupled device [EM-CCD]). The frames were then processed with the NanoJ-SRRF software[41] (a plug-in for ImageJ) to generate a super-resolution temporal reconstructed image. Figure 3 shows the results obtained in standard TIRF (Figures 3A–3F) using the above-mentioned EM-CCD camera (intensity averaging of 100 frames), and the corresponding images were obtained with the SRRF analysis method (Figures 3G–3L).

SRRF images show the details of fiber morphology that are not detectable with conventional fluorescence imaging techniques. The fluorescence intensity cross-section of the fibers of the Gel@TCPP 0.012 mM and Gel@TCPP 0.12 mM obtained with SRRF (Figures 3M and 3N) displays an apparent FWHM of 80–110 nm, a 4-fold improvement with respect to conventional TIRF imaging. In addition, SRRF analysis suggests an interesting change in fiber morphology when the gel is loaded with the highest TCPP concentration (1.2 mM), highlighting the tendency of the fibers to form large bundles and clusters. In fact, the SRRF image obtained for the sample Gel@TCPP 1.2 mM seems to reveal that fibers are made of multiple strands that run parallel to each other, twisting and intertwining into larger bundles. The intensity cross-section profile of Gel@TCPP 1.2 mM shown in Figure 3O unveils 3 different fiber strands, with the Gaussian fit giving apparent FWHMs of 32, 40, and 42 nm (with distance between fluorescence intensity maxima of 45 nm), which is a 10-fold improvement in resolution with respect to standard TIRF.

These features clearly indicate that the porphyrin load is crucial in determining fiber morphology, which changes for relatively high concentrations of TCPP. This behavior was confirmed by powder X-ray diffraction (XRD) experiments (Figure S4) and scanning electron microscopy (SEM) analysis (*vide infra*).

Structure and Morphology

The powder diffractograms were acquired on xerogels obtained from gels in water:ethanol 1:1 without porphyrin and with the 3 TCPP concentrations noted above (see Figure S4). All of the xerogels have similar diffraction peak positions, which is essentially independent of the TCPP loading. There is a difference in the intensity of the diffraction peaks, presumably because of differing morphology and long-range order in the fibers. The diffractogram of the xerogel of 1.2Br with no incorporated TCPP (black line) displays the same features previously reported,[39] which highlight the lamellar arrangement that the amphiphile adopts within the fibers. In particular, the most intense peak centered at 2θ values of $\approx 2.3^{\circ}$ (corresponding to a d-spacing of 3.85 nm) is assigned to the periodicity of the bilayers that stack on top of one another, forming the final multilayer structure of the fibers. The diffractogram of xerogel formed with the lowest amount of porphyrin (0.012 mM, red line) does not display significant differences with respect to the one without TCPP (black line). This observation indicates that the porphyrin does not alter significantly the ordered supramolecular structure for this range of concentration. However, the gels loaded with higher amounts of TCPP (0.12 and 1.2 mM, green and blue

Figure 3. Standard TIRF versus SRRF

(A–O) Comparison between standard TIRF microscopy (A–F) with intensity averaging of 100 frames and the SRRF analysis method (G–L) of gels 12 mM in 1·2Br and 0.012 mM (A, D, G, and J), 0.12 mM (B, E, H, and K), and 1.2 mM (C, F, I, and L) in TCPP. Blue squares indicate the magnifications of the same areas of the samples analyzed with the 2 modalities, with dashed red lines representing the positions of cross-section profiles reported at the bottom. In the bottom row (M–O), experimental fluorescence intensity data (circles) and Gaussian fits (lines) of cross-sections obtained with standard TIRF (red) and SRRF (black, and total fit in blue) measurements. The scale bars in the micrographs represent 5 μm (0.5 μm in magnified images).

Please cite this article in press as: Samperi et al., Enhancing Singlet Oxygen Generation by Self-Assembly of a Porphyrin Entrapped in Supramolecular Fibers, Cell Reports Physical Science (2020), https://doi.org/10.1016/j.xcrp.2020.100030

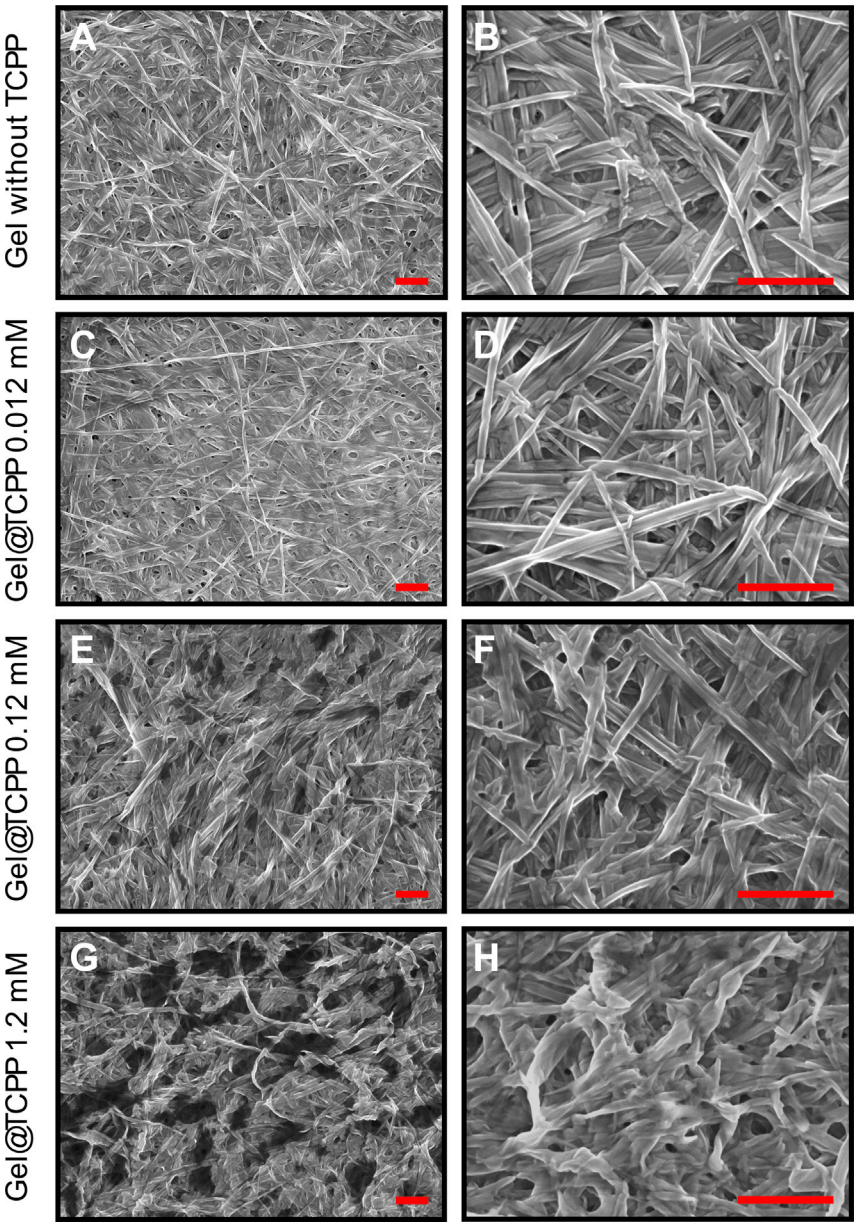

Figure 4. Morphology of Gel@TCPP by SEM

(A–H) SEM micrographs at 2 different magnifications of xerogels made from gels at a 12 mM concentration of 1·2Br in a water-ethanol ratio 1:1, without porphyrin (A and B), and with TCPP 0.012 mM (C and D), 0.12 mM (E and F), and 1.2 mM (G and H). The scale bars in the micrographs represent 1 μm.

lines, respectively), show a progressive decrease in the intensity of all peaks, indicating that this porphyrin load affects very significantly the long-range amphiphile packing and fiber morphology. These features support the observations of the morphology of the fibers obtained by SEM (Figure 4).

The SEM micrographs acquired from xerogels resulting from gels made with 1.2Br and its combinations with TCPP show significant differences in fiber morphology and their mutual arrangement. The xerogel without TCPP displays well-defined

Please cite this article in press as: Samperi et al., Enhancing Singlet Oxygen Generation by Self-Assembly of a Porphyrin Entrapped in Supramolecular Fibers, Cell Reports Physical Science (2020), https://doi.org/10.1016/j.xcrp.2020.100030

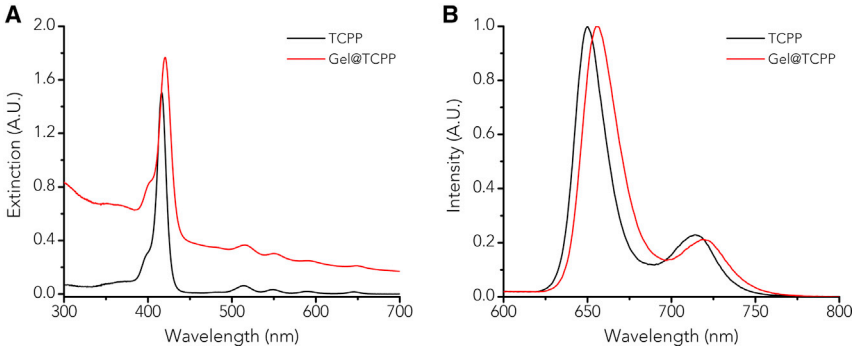

Figure 5. Photophysical Properties of TCPP and Gel@TCPP

(A and B) Extinction (A) and normalized fluorescence emission (B) spectra of TCPP in a water-ethanol ratio 1:1 (black curve) and within the gel in a water-ethanol ratio 1:1 (red curve). Experimental conditions: TCPP = 20 μM, 1·2Br = 12 mM, λ_{Exc} = 330 nm, long-pass filter 395 nm.

micrometric-long fibers of variable size, spanning from 50 to 200 nm in width, with large fibers visibly comprising multiple narrow strands aligned in straight and flat nanoribbons. The presence of low amount of TCPP (0.012 mM) into the gel does not cause significant variation in the morphology of the fibers obtained by SEM, in line with powder XRD data (Figure S4). When the gel is loaded with TCPP 0.12 and 1.2 mM, fiber morphology drastically changes, showing fibers that start to appear much less flat and less defined, with a high tendency to cluster and form large intertwined bundles for TCPP 1.2 mM. Therefore, the long-range order in the fibers is disturbed by the presence of 1.2 mM TCPP, leading to a more twisted and linked network, which is consistent with SRRF analysis.

Photophysical Properties and SO Generation

UV-visible (UV-vis) absorption and fluorescence spectroscopies were used to gain further insights into the physicochemical properties of the porphyrin within the gel. Figure 5 shows the extinction and emission spectra of the TCPP 20 μM in a 1:1 water-ethanol mixture and incorporated within the gel formed with 1·2Br 12 mM and the same solvent ratio. The extinction spectrum of the porphyrin in solution displays the typical features of this class of molecules: an intense Soret band that is centered at 417 nm with shoulder at 400 nm and a set of 4 weak but well-defined Q-bands characteristic of a D_{2h} symmetry, centered at 514, 549, 590, and 645 nm. These features do not change significantly when the porphyrin is trapped within the gel. The extinction spectrum of Gel@TCPP shows an increase in the baseline due to the light scattered by the fibrillar network of the gel, together with a modest bathochromic shift of all of the bands of 2–4 nm, with the Soret band now centered at 421 nm and the Q-bands at 516, 551, 593, and 649 nm. The fluorescence emission spectra of the 2 samples also show a similar behavior. TCPP emission in water-ethanol 1:1 is characterized by 2 broad bands, with the most intense band centered at 650 nm and the less intense band at 714 nm. Similar to that seen by extinction spectroscopy, a modest bathochromic shift (6 nm) is observed when the porphyrin is incorporated into the gel, with the 2 bands now centered at 656 and 720 nm. It has been reported that the UV-vis and fluorescent properties of TCPP are highly dependent on the solvent properties and the ionic strength, which affect the degree of aggregation of this porphyrin. More specifically, the ionized TCPP (carboxylate form) in aqueous solution at pH 7.0 or higher and at low concentration (<1 μM) is considered to be in a non-aggregated form, with deviations from Beer's law at higher concentrations generally ascribed to the formation of dimers or higher aggregates.[42,43]

Please cite this article in press as: Samperi et al., Enhancing Singlet Oxygen Generation by Self-Assembly of a Porphyrin Entrapped in Supramolecular Fibers, Cell Reports Physical Science (2020), https://doi.org/10.1016/j.xcrp.2020.100030

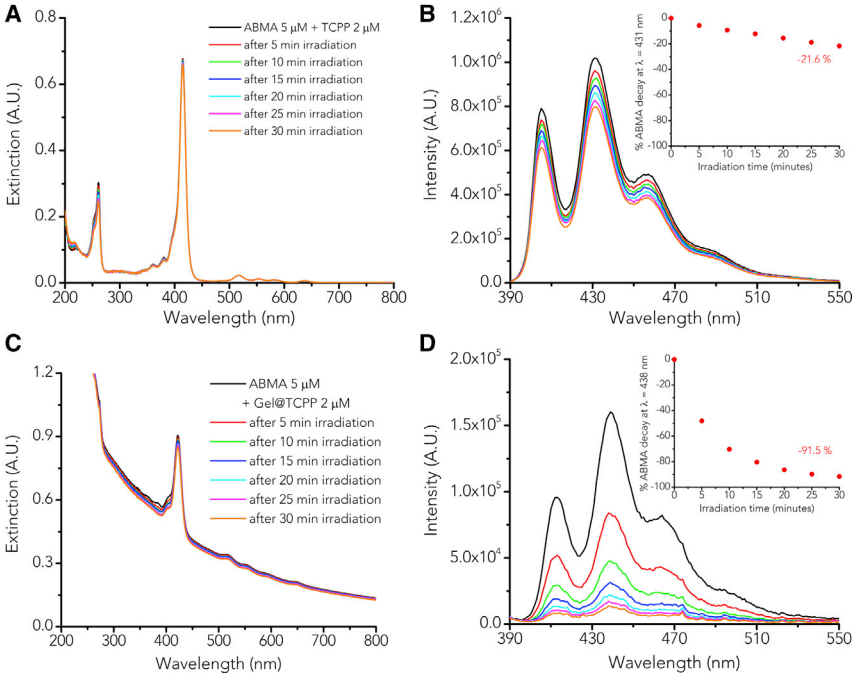

Figure 6. SO Generationzfrom TCPP and Gel@TCPP

(A–D) Extinction (A and C) and fluorescence emission (B and D) spectra of ABMA in the presence of TCPP (A and B) and after addition of Gel@TCPP (C and D), followed by irradiation for 30 min with spectra acquisition every 5 min. Insets: percentage decrease in emission fluorescence intensity of ABMA recorded upon irradiation. Experimental conditions: ABMA = 5 μM, PBS = 2 mM at pH = 7.4, TCPP = 2 μM. Gel formulation: 1·2Br = 12 mM, TCPP = 20 μM and water-ethanol ratio 1:1. The final TCPP concentration in solution is 2 μM, with ethanol content of 5%. λ_{Exc} = 380 nm, long-pass filter 395 nm. Irradiation condition: 0.3 sun (30 mW/cm^2), long-pass filter at 495 nm and a 10-cm-thick water filter.

The precise position of the Soret band of TCPP can change significantly as a function of the polarity of the medium and the salt addition, with more polar mixtures and high ionic strengths leading to blue shift and decrease in absorptivity, which is generally ascribed to the formation of small aggregates, although at the concentrations used here, the aggregation is considered minimal.[44] This behavior is clearly shown in the absorption spectra of TCPP 20 μM in pure water and water-ethanol mixtures with different ratios of the 2 solvents (Figure S5). As the amount of ethanol in the mixture increases, the Soret band shows a progressive increase in absorptivity with a bathochromic shift of 2 nm, together with sharpening of the Q-bands and changing in their positions. In parallel, the fluorescence emission spectra show a modest bathochromic shift and an increase in intensity of the 2 bands that become less broad. The behaviors observed as a function of the ethanol content are ascribable to a reduction in minor aggregation of the porphyrin in water-rich solvent mixtures, a feature that is also maintained when the TCPP is incorporated into the gel.

The ability of TCPP to generate SO under irradiation was assessed using 9,10-anthracenedyl-bis(methylene)dimalonic acid (ABMA) as a molecular probe, an anthracene derivative that is commonly used for this purpose.[45] In the presence of SO, ABMA is oxidized into an endoperoxide, leading to an observed decrease in the fluorescence emission in the region of the probe. This combination of materials is quite specific to SO, although small amounts of other ROS may be generated. To study SO production, the emission decrease (reflecting the concentration decrease)

Please cite this article in press as: Samperi et al., Enhancing Singlet Oxygen Generation by Self-Assembly of a Porphyrin Entrapped in Supramolecular Fibers, Cell Reports Physical Science (2020), https://doi.org/10.1016/j.xcrp.2020.100030

Cell Reports
Physical Science

CellPress

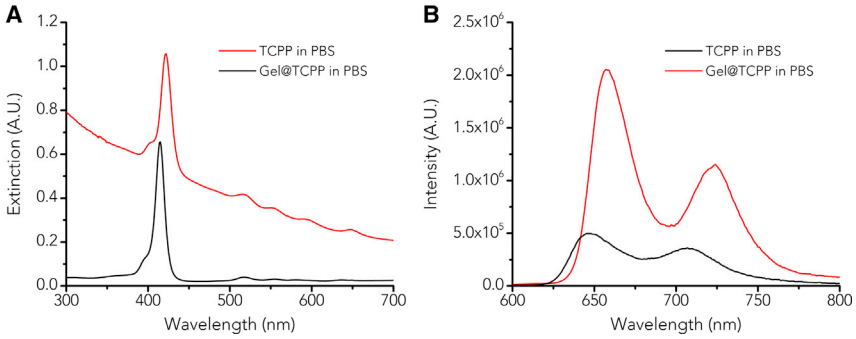

Figure 7. Photophysical Properties of TCPP and Gel@TCPP in PBS

(A and B) Extinction (A) and fluorescence emission (B) spectra of TCPP (black curve) and Gel@TCPP (red curve) in PBS 2 mM, pH = 7.4. Gel formulation: 1·2Br = 12 mM, TCPP = 20 μM and water-ethanol ratio 1:1. The final TCPP concentration for both samples is 2 μM, with ethanol content of 5%. λ_{Exc} = 330 nm, long-pass filter 395 nm.

in ABMA was evaluated in the presence of TCPP as a homogeneous solution and when incorporated into the gel (see Experimental Procedures for further details). The samples were irradiated for 30 min at 0.3 sun (30 mW/cm^2, with a long-pass filter at 495 nm to remove the UV component and a 10-cm-thick water filter to remove the infrared [IR] portion of the spectrum), and extinction and fluorescence emission spectra were recorded every 5 min (Figure 6). In the presence of TCPP in solution, a moderate decrease in the absorption bands of ABMA is observed, in parallel with a gradual decrease in its fluorescence emission, which shows a degradation of ABMA of 21.6% (Figures 6A and 6B).

When TCPP was incorporated into the gel fibers, UV-vis extinction spectra showed the presence of TCPP and ABMA together with a significant scattering contribution caused by the colloid in suspension (Figure 6C). Upon irradiation, ABMA absorption bands decrease remarkably, indicating high SO generation, a feature that is more evident from the decay of the fluorescence emission, which shows a degradation of ABMA of 91.5% (Figure 6D).

To compare the degradation rates of ABMA obtained in the presence of TCPP in solution and when delivered as Gel@TCPP, we analyzed the 2 degradation profiles as pseudo-first order processes for the early part of the reaction (TCPP concentration remains constant over the irradiation time), and the results are shown in Figure S6. The rate constants obtained from the fits show that Gel@TCPP is able to accelerate the reaction between ABMA and SO by a factor of 14 when compared with dissolved TCPP.

Control experiments of only ABMA without TCPP and in the presence of the gel 1·2Br display only a minor degradation of ABMA under irradiation under the same experimental conditions, showing a decrease in fluorescence emission of 7.5% with respect to the initial intensity after 30 min, confirming no relevant SO production when the photosensitizer is absent (Figure S7). The addition of the gel to the ABMA leads to an increase in the scattered light arising from the dispersion of the fibers in solution (Figure S7A), together with a significant bathochromic shift (6–7 nm) and decrease in the fluorescence emission of ABMA (Figure S7B). A similar bathochromic shift was already observed for the interaction of TCPP with the gel fibers, and it is ascribable to an electrostatic interaction between the anthracene derivative, which is negatively charged under these experimental conditions, and fibers of the gel that possess a positively charged surface.

Cell Reports
Physical Science

CellPress

Figure 7 shows the extinction and fluorescence spectra of TCPP and Gel@TCPP in PBS solution, the same experimental conditions adopted to evaluate the SO generation. TCPP in PBS possesses very similar features compared to those in water: the extinction spectrum displays the Soret band at 415 nm and the Q-bands at 517, 554, 580, and 636 nm, while the fluorescence emission spectrum shows 2 broad bands centered at 647 and 707 nm. These features change significantly when the porphyrin is incorporated into the gel fibers. Both mixtures are stable over at least a period of days (Figure S8). The Soret band undergoes a significant bathochromic shift and is now centered at 422 nm, similar to the Q-bands, which show their maxima at 518, 555, 595, and 649 nm. In parallel, the 2 fluorescence emission bands show a similar bathochromic shift (now centered at 658 and 723 nm) and become less broad and more intense, indicating a reduction in the degree of aggregation comparable to that observed in ethanol-rich solvent mixtures.

DISCUSSION

In conclusion, the simplicity and efficiency of the formation of the hybrid nanomaterial described here along with its high SO-forming ability under illumination bodes well for its application in several areas highlighted at the beginning of the article. The structure of the fibers in the vicinity of the porphyrin has been revealed using SRRF microscopy, demonstrating that the porphyrin is confined to the gel fibers in a robust way, with rows of porphyrins that presumably align with the lamellae formed by the gelator. The exact location of the porphyrins within the fibers has been observed, although it is not possible to identify conclusively the photosensitizers that are on the faces or edges of the fibers, which are presumably the most important for the function described herein. The nanomaterial is unique in its enhanced efficiency as a photosensitizer for the formation of SO (14-fold improvement compared to the free porphyrin in solution), as well as its stability for a supramolecular system, presumably as a result of the specific electrostatic interactions between the porphyrin and the gelator. For example, unlike a hydrogel system based on the incorporation of sodium 5-(4-aminophenyl)-10,15,20-tris-(4-sulfonatophenyl) porphyrin into silk fibroin where porphyrins are released,[46] the nanomaterial reported here is robust, no release of photosensitizer occurs (and under the proportions used all the porphyrin is bound in the fibers), and it provides sustained photosensitizer activity in suspension. The increase in SO generation is not only a result of avoiding porphyrin aggregation, because in solution the sample is not aggregated significantly (unlike other nanomaterials[47]), and therefore the specific immobilization geometries must be a determining factor. The electrostatic nature of the co-assembly is potentially highly versatile and promising for the preparation of similar nanomaterials with multifunctional behaviors.

EXPERIMENTAL PROCEDURES

Materials

All reagents and solvents used in this work were of analytical grade. Sodium hydroxide (NaOH) was purchased from Merck (Germany). Phosphate buffered saline (PBS) tablets and 9,10-anthracenedyl-bis(methylene)dimalonic acid (ABMA) came from Sigma-Aldrich.

Milli-Q water (obtained with the Milli-Q Plus system from Millipore) was used for the preparation of all of the samples. Compound 1,3-bis[(3-octadecyl-1-imidazolio)methyl]benzene dibromide was synthesized as previously reported in the literature.[48] TCPP was synthesized, adopting the synthetic protocol reported here.[49]

Please cite this article in press as: Samperi et al., Enhancing Singlet Oxygen Generation by Self-Assembly of a Porphyrin Entrapped in Supramolecular Fibers, Cell Reports Physical Science (2020), https://doi.org/10.1016/j.xcrp.2020.100030

Gel Preparation

Where it is not specified differently, gels 12 mM in 1.2Br were made by mixing ethanol solutions of the gelator and Milli-Q water solutions containing the appropriate amount of NaTCPP as total volume 1-mL samples in 3-mL closed vials, sealed after gentle mixing (with a micropipette) and letting them stand undisturbed at room temperature to allow gel formation (Video S1). Gels were deemed to have formed when no flow was observed upon the vial-inversion test. For porphyrin-containing gels, an aqueous solution of porphyrin as sodium salt was prepared by dispersing the desired amount of solid TCPP in water, followed by the addition of 4 equivalents of sodium hydroxide (from 0.1 M stock solution).

Gel Characterization

The rheological analysis was performed using an Anton Paar MCR 302 rheometer equipped with a temperature controller and parallel plate geometry setup (PP50 stainless steel, 50 mm diameter, 1-mm gap between plates). All of the measurements were carried out at 298 K. Samples were prepared as 6 mL total volume in 7-cm diameter Petri dishes and sealed to prevent solvent evaporation. Gels were kept at room temperature for 2 days before study. Samples were carefully transferred on the rheometer plate without breakage and the extra material was removed to suit the working geometry. Resistance to deformation and resistance to rupture were evaluated while performing oscillation amplitude tests at deformation frequency $\nu = 1$ Hz.

Fluorescence imaging was carried out on a Zeiss Elyra PS1 super-resolution microscope equipped with Zen 2012 acquisition and processing software, fitted with an alpha Plan-Apochromat 100×/1.46 Oil DIC M27 Elyra objective lens operating in TIRF, 405 nm laser (50 mW), and LP 650 filter. A droplet of 30°C oil (Zeiss, Immersol 518F/30°) was placed on the objective lens before imaging. Automatic focusing was used to maintain the desired focal plane during the acquisition. Images were acquired with a pco.edge scientific CMOS (sCMOS) camera using the "16 Avg" option in TIRF mode (mirror angle 66.92°), at 2% laser power and a camera exposure time of 200 ms. SRRF images were obtained, acquiring 100 image frames (or cycles) in TIRF mode (mirror angle 71.50°) using 0.5% laser power, recorded with an EM-CCD (Andor EM-CCD camera iXon Du 897) with 200 gain and 25-ms exposure time per frame. Image processing was carried out with Fiji image analysis software,[50] and the SRRF analysis was performed using the open-source NanoJ-SRRF software package.[36] The algorithm used was temporal radiality pairwise product mean (TRPPM), and the optimized parameters were a ring radius of 0.5, a radiality magnification of 10, and 6 axes in a ring, with intensity weighting and gradient smoothing.

Powder XRD patterns were obtained by a PANalytical MPD X-Ray Powder Diffractometer in Bragg-Brentano geometry, using Cu-Kα radiation (Kα1 = 1.540560 Å and Kα2 = 1.544390 Å) with a voltage and current of 40 kV and 40 mA, respectively. A total of 3 mL gel was prepared for each sample analyzed; these were dried under reduced pressure to obtain xerogels. The powder was collected and placed on a brass sample holder for data acquisition in 2θ scale between 2° and 30°, with a step size of 0.013°.

SEM images were acquired with a JEOL 7100F FEG-SEM system on samples cast on aluminum stubs, dried under vacuum (fast drying achieved within 5–10 s after casting to minimize possible drying effects), and coated with a 5-nm-thick layer of iridium. Image acquisition was performed using a working distance of 6 mm and 5 kV accelerating voltage.

Cell Reports
Physical Science

UV-vis extinction spectroscopy was performed using a Cary 5000 UV-vis spectrophotometer (Agilent). Fluorescence spectroscopy was measured using an FLS 980 spectrometer (Edinburgh Instruments) equipped with a front face sample holder. The measurements were carried out using quart cuvettes having a 2 or 10 mm path length.

SO Generation

SO production was measured by monitoring the fluorescence decrease of ABMA in a 2-mM PBS solution at pH 7.4 in the presence of NaTCPP and Gel@TCPP upon irradiation. The molar ratio of ABMA and porphyrin was kept constant (2.5:1) for each sample. A 10-mm cuvette containing the sample was irradiated using a xenon lamp with a long-pass filter at 495 nm, a 10-cm-thick water filter to remove the IR portion of the spectrum, at 0.3 sun (30 mW/cm^2) for 30 min (Figure S9). Fluorescence emission spectra were recorded at 5-min intervals.

In a typical irradiation experiment, an aliquot of 250 μL containing either the photosensitizer in water:ethanol 1:1 or a gel with TCPP obtained with the same solvent mixture (see Videos S2 and S3 for preparation), was added to a 2,250-μL solution of ABMA 5 μM in PBS 2 mM at pH = 7.4, to give a final TCPP concentration of 2 μM and a final ethanol content of 5%.

DATA AND CODE AVAILABILITY

All of the data associated with the study are included in the paper and the supplemental information.

SUPPLEMENTAL INFORMATION

Supplemental Information can be found online at https://doi.org/10.1016/j.xcrp.2020.100030.

ACKNOWLEDGMENTS

This work was supported by the Engineering and Physical Sciences Research Council (EPSRC) under grants EP/M005178/1 and EP/N024818/1, European Regional Development Fund (FEDER) funds, Spanish government grant TEC 2017-85059-C3-2-R, and the University of Nottingham. The authors thank the Nanoscale and Microscale Research Centre (nmRC) and the School of Life Sciences Imaging (SLIM), in particular Robert Markus, in Nottingham. We thank warmly Brian Amabilino i Pérez and Adrià Amabilino i Pérez who helped MS with preliminary experiments.

AUTHOR CONTRIBUTIONS

Conceptualization, M.S., L.P.-G., and D.B.A.; Methodology, M.S., L.P.-G., and D.B.A.; Investigation, M.S. and D.L.; Writing – Original Draft, M.S., L.P.-G., and D.B.A.; Writing – Review & Editing, M.S., D.L., L.P.-G., and D.B.A.; Funding Acquisition, D.B.A. and L.P.-G.; Resources, L.P.-G. and D.B.A.

DECLARATION OF INTERESTS

The authors declare no competing interests.

Received: December 11, 2019
Revised: January 10, 2020
Accepted: January 24, 2020
Published: March 11, 2020

Cell Reports
Physical Science

CellPress

REFERENCES

1. Li, Q., Mahendra, S., Lyon, D.Y., Brunet, L., Liga, M.V., Li, D., and Alvarez, P.J.J. (2008). Antimicrobial nanomaterials for water disinfection and microbial control: potential applications and implications. Water Res. *42*, 4591–4602.

2. Moloney, J.N., and Cotter, T.G. (2018). ROS signalling in the biology of cancer. Semin. Cell Dev. Biol. *80*, 50–64.

3. Garcia-Fresnadillo, D. (2018). Singlet Oxygen Photosensitizing Materials for Point-of-Use Water Disinfection with Solar Reactors. ChemPhotoChem. *2*, 512–534.

4. Pibiri, I., Buscemi, S., Palumbo-Piccionello, A., and Pace, A. (2018). Photochemically Produced Singlet Oxygen: Applications and Perspectives. ChemPhotoChem *2*, 535–547.

5. Janků, M., Luhová, L., and Petřivalský, M. (2019). On the Origin and Fate of Reactive Oxygen Species in Plant Cell Compartments. Antioxidants *8*, 105.

6. Longevial, J.F., Clément, S., Wytko, J.A., Ruppert, R., Weiss, J., and Richeter, S. (2018). Peripherally Metalated Porphyrins with Applications in Catalysis, Molecular Electronics and Biomedicine. Chemistry *24*, 15442–15460.

7. Ghogare, A.A., and Greer, A. (2016). Using Singlet Oxygen to Synthesize Natural Products and Drugs. Chem. Rev. *116*, 9994–10034.

8. Wu, L., Lee, D.S., Boufroura, H., Poliakoff, M., and George, M.W. (2018). Photooxidation of Fulvenes in a Continuous Flow Photoreactor using Carbon Dioxide as a Solvent. ChemPhotoChem *2*, 580–585.

9. Yu, Q., Zhang, Y.T., and Wan, J.P. (2019). Ambient and aerobic carbon–carbon bond cleavage toward α-ketoester synthesis by transition-metal-free photocatalysis. Green Chem. *21*, 3436–3441.

10. Redmond, R.W., and Gamlin, J.N. (1999). A compilation of singlet oxygen yields from biologically relevant molecules. Photochem. Photobiol. *70*, 391–475.

11. Mathai, S., Smith, T.A., and Ghiggino, K.P. (2007). Singlet oxygen quantum yields of potential porphyrin-based photosensitisers for photodynamic therapy. Photochem. Photobiol. Sci. *6*, 995–1002.

12. Li, X., Lee, S., and Yoon, J. (2018). Supramolecular photosensitizers rejuvenate photodynamic therapy. Chem. Soc. Rev. *47*, 1174–1188.

13. Cheng, H.B., Cui, Y.X., Wang, R., Kwon, N., and Yoon, J. (2019). The development of light-responsive, organic dye based, supramolecular nanosystems for enhanced anticancer therapy. Coord. Chem. Rev. *392*, 237–254.

14. Roy, I., Bobbala, S., Young, R.M., Beldjoudi, Y., Nguyen, M.T., Cetin, M.M., Cooper, J.A., Allen, S., Anamimoghadam, O., Scott, E.A., et al. (2019). A Supramolecular Approach for Modulated Photoprotection, Lysosomal Delivery, and Photodynamic Activity of a Photosensitizer. J. Am. Chem. Soc. *141*, 12296–12304.

15. Adarsh, N., Babu, P.S.S., Avirah, R.R., Viji, M., Nair, S.A., and Ramaiah, D. (2019). Aza-BODIPY nanomicelles as versatile agents for the in vitro and in vivo singlet oxygen-triggered apoptosis of human breast cancer cells. J. Mater. Chem. B Mater. Biol. Med. *7*, 2372–2377.

16. Han, J., Liu, K., Chang, R., Zhao, L., and Yan, X. (2019). Photooxidase-Mimicking Nanovesicles with Superior Photocatalytic Activity and Stability Based on Amphiphilic Amino Acid and Phthalocyanine Co-Assembly. Angew. Chem. Int. Ed. Engl. *58*, 2000–2004.

17. García Calavia, P., Bruce, G., Pérez-García, L., and Russell, D.A. (2018). Photosensitiser-gold nanoparticle conjugates for photodynamic therapy of cancer. Photochem. Photobiol. Sci. *17*, 1534–1552.

18. Amara, Z., Bellamy, J.F.B., Horvath, R., Miller, S.J., Beeby, A., Burgard, A., Rossen, K., Poliakoff, M., and George, M.W. (2015). Applying green chemistry to the photochemical route to artemisinin. Nat. Chem. *7*, 489–495.

19. Hamami, Z.E., Vanoye, L., Fongarland, P., de Bellefon, C., and Favre-Réguillon, A. (2019). Improved Reactor Productivity for the Safe Photo-Oxidation of Citronellol Under Visible Light LED Irradiation. ChemPhotoChem *3*, 122–128.

20. Hone, C.A., and Kappe, C.O. (2019). Correction to: The Use of Molecular Oxygen for Liquid Phase Aerobic Oxidations in Continuous Flow. Top. Curr. Chem. *377*, 7.

21. Bonnett, R. (1995). Photosensitizers of the porphyrin and phthalocyanine series for photodynamic therapy. Chem. Soc. Rev. *24*, 19–33.

22. Antoni, P.M., Naik, A., Albert, I., Rubbiani, R., Gupta, S., Ruiz-Sanchez, P., Munikorn, P., Mateos, J.M., Luginbuehl, V., Thamyongkit, P., et al. (2015). (Metallo)porphyrins as potent phototoxic anti-cancer agents after irradiation with red light. Chemistry *21*, 1179–1183.

23. Wang, H., Yu, D., Fang, J., Cao, C., Liu, Z., Ren, J., and Qu, X. (2019). Renal-Clearable Porphyrinic Metal-Organic Framework Nanodots for Enhanced Photodynamic Therapy. ACS Nano *13*, 9206–9217.

24. Jenni, S., Sour, A., Bolze, F., Ventura, B., and Heitz, V. (2019). Tumour-targeting photosensitisers for one- and two-photon activated photodynamic therapy. Org. Biomol. Chem. *17*, 6585–6594.

25. Lavado, A.S., Chauhan, V.M., Zen, A.A., Giuntini, F., Jones, D.R.E., Boyle, R.W., Beeby, A., Chan, W.C., and Aylott, J.W. (2015). Controlled intracellular generation of reactive oxygen species in human mesenchymal stem cells using porphyrin conjugated nanoparticles. Nanoscale *7*, 14525–14531.

26. Figueira, F., Cavaleiro, J.A.S., and Tomé, J.P.C.C. (2011). Silica nanoparticles functionalized with porphyrins and analogs for biomedical studies. J. Porphyr. Phthalocyanines *15*, 517–533.

27. Bruce, G., Samperi, M., Amabilino, D.B., Duch, M., Plaza, J.A., and Pérez-García, L. (2019). Singlet oxygen generation from porphyrin-functionalized hexahedral polysilicon microparticles. J. Porphyr. Phthalocyanines *23*, 223–233.

28. Yang, C.J., Gao, L.C., Zhang, B.G., Zhang, Z.H., and Deng, K.J. (2018). Uniform zinc thioporphyrazine nanosphere by self-assembly and the photocatalytic performance. J. Porphyr. Phthalocyanines *22*, 868–876.

29. Fernandez, L., Esteves, V.I., Cunha, A., Schneider, R.J., and Tomé, J.P.C.C. (2016). Photodegradation of organic pollutants in water by immobilized porphyrins and phthalocyanines. J. Porphyr. Phthalocyanines *20*, 150–166.

30. Neves, C.M.B., Filipe, O.M.S., Mota, N., Santos, S.A.O., Silvestre, A.J.D., Santos, E.B.H., Neves, M.G.P.M.S., and Simões, M.M.Q. (2019). Photodegradation of metoprolol using a porphyrin as photosensitizer under homogeneous and heterogeneous conditions. J. Hazard. Mater. *370*, 13–23.

31. Scanone, A.C., Gsponer, N.S., Alvarez, M.G., and Durantini, E.N. (2017). Photodynamic properties and photoinactivation of microorganisms mediated by 5,10,15,20-tetrakis(4-carboxyphenyl)porphyrin covalently linked to silica-coated magnetite nanoparticles. J. Photochem. Photobiol. Chem. *346*, 452–461.

32. Xia, L.-Y., Zhang, X., Cao, M., Chen, Z., and Wu, F.-G. (2017). Enhanced Fluorescence Emission and Singlet Oxygen Generation of Photosensitizers Embedded in Injectable Hydrogels for Imaging-Guided Photodynamic Cancer Therapy. Biomacromolecules *18*, 3073–3081.

33. Feng, X., Liu, C., Wang, X., Jiang, Y., Yang, G., Wang, R., Zheng, K., Zhang, W., Wang, T., and Jiang, J. (2019). Functional Supramolecular Gels Based on the Hierarchical Assembly of Porphyrins and Phthalocyanines. Front Chem. *7*, 336.

34. Belali, S., Savoie, H., O'Brien, J.M., Cafolla, A.A., O'Connell, B., Karimi, A.R., Boyle, R.W., and Senge, M.O. (2018). Synthesis and Characterization of Temperature-Sensitive and Chemically Cross-Linked Poly(N-isopropylacrylamide)/Photosensitizer Hydrogels for Applications in Photodynamic Therapy. Biomacromolecules *19*, 1592–1601.

35. Chambre, L., Saw, W.S., Ekineker, G., Kiew, L.V., Chong, W.Y., Lee, H.B., Chung, L.Y., Bretonnière, Y., Dumoulin, F., and Sanyal, A. (2018). Surfactant-Free Direct Access to Porphyrin-Cross-Linked Nanogels for Photodynamic and Photothermal Therapy. Bioconjug. Chem. *29*, 4149–4159.

36. Gustafsson, N., Culley, S., Ashdown, G., Owen, D.M., Pereira, P.M., and Henriques, R. (2016). Fast live-cell conventional fluorophore nanoscopy with ImageJ through super-resolution radial fluctuations. Nat. Commun. *7*, 12471.

37. Rodrigues, M., Calpena, A.C., Amabilino, D.B., Garduño-Ramirez, M.L., and Pérez-García, L.

(2014). Supramolecular gels based on a gemini imidazolium amphiphile as molecular material for drug delivery. J. Mater. Chem. B Mater. Biol. Med. *2*, 5419–5429.

38. Limón, D., Amirthalingam, E., Rodrigues, M., Halbaut, L., Andrade, B., Garduño-Ramírez, M.L., Amabilino, D.B., Pérez-García, L., and Calpena, A.C. (2015). Novel nanostructured supramolecular hydrogels for the topical delivery of anionic drugs. Eur. J. Pharm. Biopharm. *96*, 421–436.

39. Samperi, M., Pérez-García, L., and Amabilino, D.B. (2019). Quantification of energy of activation to supramolecular nanofibre formation reveals enthalpic and entropic effects and morphological consequence. Chem. Sci. *10*, 10256–10266.

40. Ambrose, E.J. (1956). A surface contact microscope for the study of cell movements. Nature *178*, 1194.

41. Culley, S., Tosheva, K.L., Matos Pereira, P., and Henriques, R. (2018). SRRF: universal live-cell super-resolution microscopy. Int. J. Biochem. Cell Biol. *101*, 74–79.

42. Pasternack, R.F., Huber, P.R., Boyd, P., Engasser, G., Francesconi, L., Gibbs, E., Fasella, P., Venturo, G.C., and Hinds, Lde.C. (1972). On the aggregation of meso-substituted water-soluble porphyrins. J. Am. Chem. Soc. *94*, 4511–4517.

43. White, W.I. (1978). Aggregation of Porphyrins and Metalloporphyrins. In The Porphyrins, D. Dolphin, ed. (Academic Press), pp. 303–339.

44. Clarke, S.E., Wamser, C.C., and Bell, H.E. (2002). Aqueous Complexation Equilibria of meso-Tetrakis(4-carboxyphenyl)porphyrin with Viologens: Evidence for 1:1 and 1:2 Complexes and Induced Porphyrin Dimerization. J. Phys. Chem. A *106*, 3235–3242.

45. Alea-Reyes, M.E., Penon, O., García Calavia, P., Marín, M.J., Russell, D.A., and Pérez-García, L. (2018). Synthesis and in vitro phototoxicity of multifunctional Zn(II)meso-tetrakis(4-carboxyphenyl)porphyrin-coated gold nanoparticles assembled via axial coordination with imidazole ligands. J. Colloid Interface Sci. *521*, 81–90.

46. Rojas, J.E.U., Gerbelli, B.B., Ribeiro, A.O., Nantes-Cardoso, I.L., Giuntini, F., and Alves, W.A. (2019). Silk fibroin hydrogels for potential applications in photodynamic therapy. Biopolymers *110*, e23245.

47. Wang, J., Zhong, Y., Wang, X., Yang, W., Bai, F., Zhang, B., Alarid, L., Bian, K., and Fan, H. (2017). pH-Dependent Assembly of Porphyrin-Silica Nanocomposites and Their Application in Targeted Photodynamic Therapy. Nano Lett. *17*, 6916–6921.

48. Casal-Dujat, L., Rodrigues, M., Yagüe, A., Calpena, A.C., Amabilino, D.B., González-Linares, J., Borràs, M., and Pérez-García, L. (2012). Gemini imidazolium amphiphiles for the synthesis, stabilization, and drug delivery from gold nanoparticles. Langmuir *28*, 2368–2381.

49. Datta-Gupta, N., and Bardos, T.J. (1966). Synthetic Porphyrins. I. Synthesis and Spectra of some *para*-Substituted meso-Tetraphenylporphines. J. Heterocyc. Chem. *3*, 495–502.

50. Schindelin, J., Arganda-Carreras, I., Frise, E., Kaynig, V., Longair, M., Pietzsch, T., Preibisch, S., Rueden, C., Saalfeld, S., Schmid, B., et al. (2012). Fiji: an open-source platform for biological-image analysis. Nat. Methods *9*, 676–682.